Engineering Fracture Mechanics 98 (2013) 52–63

Contents lists available at SciVerse ScienceDirect

Engineering Fracture Mechanics

journal homepage: www.elsevier.com/locate/engfracmech

Fracture testing of the heat affected zone from welded steel pipes using an in situ stage

Gustavo M. Castelluccio [a,*], Juan E. Perez Ipiña [b,c], Alejandro A. Yawny [b,d], Hugo A. Ernst [e]

[a] The George W. Woodruff School of Mechanical Engineering, Georgia Institute of Technology, Atlanta, GA 30332-0405, USA
[b] Consejo Nacional de Investigaciones Científicas y Técnicas (CONICET), Argentina
[c] Grupo Mecánica de Fractura, Universidad Nacional del Comahue, Buenos Aires 1400, 8300 Neuquen, Neuquen, Argentina
[d] División Física de Metales, Centro Atómico Bariloche (CNEA), Av. Bustillo 9500, 8400 Bariloche, Río Negro, Argentina
[e] Department of Structural Integrity, TENARIS Dr. Simini 250, Campana, Buenos Aires, Argentina

ARTICLE INFO

Article history:
Received 12 October 2011
Received in revised form 10 May 2012
Accepted 10 November 2012
Available online 14 December 2012

Keywords:
Inhomogeneity
HAZ
Weld small specimens
HSLA steel
Resistance curve

ABSTRACT

The structural assessment of welded joints requires that the weld metal and the heat-affected zone (HAZ) have adequate fracture toughness values. The measurement of these quantities is still controversial due to the inhomogeneous properties of the welds, which affects standardized methodologies. This work presents local measurements of the fracture toughness of the heat-affected zones from welded steel pipes. Fracture tests were performed inside the scanning electron microscope (SEM) using small specimens, allowing the direct measurement of the crack tip opening displacement (CTOD) on the surface. CTODs of approximately half a millimeter were attained for crack growth of about one-tenth of a millimeter before the crack crossed the fusion line. Three methods for computing the CTOD were compared, and the differences among the results were discussed. Furthermore, the surface strain field, calculated by measuring the distortion of a regular grid, showed evidence of an influence of HAZ inhomogeneity.

1. Introduction

The structural assessment of welded joints requires assuring the mechanical properties of the base material and the welded region. In particular, this work focuses on the structural integrity aspects of off-shore welded pipelines installed by means of the reeling process [1]. Here, individual pipe sections are circumferentially joined using fusion welding to produce a continuous pipeline. The reeling/unreeling processes involve severe deformation with typical values reaching 3% plastic strain. Therefore, one critical issue concerns the integrity of the welded joint upon these severe conditions.

During fusion welding, heat energy diffuses away from the weld, raises the temperature of the surrounding base material, and creates a region with steep gradients in mechanical properties. This region is referred to as the heat affected zone (HAZ) and extends for a few millimeters from the liquid–solid interface into the base metal. Fracture toughness characterization of the HAZ is a difficult task since intrinsic inhomogeneity distorts the strains around a crack. Thus, the traditional homogeneous fracture mechanics methodology may become invalid since the similitude principle may not hold and the crack tip strain fields may not be described correctly by the Hutchinson-Rice-Rosengren (HRR) model [2].

Extensive literature has documented the microstructural evolution of the HAZ region for HSLA steels in subregions with different microstructures [3]. Previous research found that the coarse grain HAZ (CGHAZ), which borders the fusion line, is a region with low toughness in high strength low alloy (HSLA) steels [4,5]. Accordingly, applicable recommendations such as

* Corresponding author.
E-mail address: castellg@gatech.edu (G.M. Castelluccio).

0013-7944/$ - see front matter © 2012 Elsevier Ltd. All rights reserved.
http://dx.doi.org/10.1016/j.engfracmech.2012.11.010

Nomenclature

HAZ	heat-affected zone
SEM	scanning electron microscope
CTOD	crack tip opening displacement
CGHAZ	coarse grain HAZ
HI	heat input
SE (B)	single-edge bending specimen
CMOD	Crack Mouth Open Displacement
LPD	Load Point Displacement
CTOA	crack tip opening angle
a	current crack length
a_o	initial crack length
d_n	proportionality constant between CTOD and J-integral
B, W, S	specimen dimensions
E^*	almansi strain tensor
E	elasticity modulus
F	applied force
n	hardening coefficient in Ramberg–Osgood law
r_p	rotation factor
U_p	work performed by the pins
α	Ramberg–Osgood constant
ε	strain
ε_o	reference strain
η_p	proportionality constant for calculating the J-integral
υ	Poisson modulus
σ	stress
σ_o	reference stress

API RP 2Z [6] call for fracture toughness tests with cracks in the CGHAZ for qualifying a weld. Considering the difficulties associated with the precise location of an artificial crack on this particular HAZ subregion, standardized procedures require the testing of several specimens accompanied by a verification of the final crack location and its trajectory.

After a large set of tensile and fracture standardized tests of welded specimens [7] were completed, questions arose about the validity of the results. The first concern regarded the location of the crack in the specimens, which has typically been solved in standards by increasing the number of tests required to qualify a weld. A second and less studied problem is related to the uncertainties of employing theoretical models based on homogeneous material to deduce the mechanical properties of the HAZ.

In a previous paper [8], we studied the tensile strength of the CGHAZ considered in this work. Here, we investigate the local behavior around the tip of a crack immersed in the same CGHAZ, which has a strong gradient in its microstructure and mechanical properties. We performed fracture tests of small specimens inside the scanning electron microscope (SEM) that allowed the direct measurement of the crack tip opening displacement (CTOD) on the surface. These measurements were compared to the computations with other methods for quantifying the CTOD, and the causes of the partial agreement were discussed. Furthermore, the influence of the HAZ inhomogeneity on the strain field on the surface of the specimens was depicted.

2. Experimental details

2.1. Material and welds

The material studied corresponds to the API X65 steel pipe for reeling applications with girth welds. The welding specifications included a root pass with a heat input (HI) of 0.8 KJ/mm and a submerged arc welding process for the filling passes

Table 1
Basic tensile properties of the pipe and weld.

	Yield strength (MPa)	Ultimate strength (MPa)	Hardening (n)
Pipe base metal	467 ± 10	570 ± 12	6.8
Weld metal 0.8 KJ/mm	581 ± 12	658 ± 14	10.3

with HIs of either 0.8 or 2.5 KJ/mm. Table 1 presents several average mechanical properties of the HSLA steel; the hardening coefficient (n) corresponds to the best fit of the experimental data using the Ramberg–Osgood law,

$$\frac{\epsilon}{\epsilon_0} = \frac{\sigma}{\sigma_0} + \alpha\left(\frac{\sigma}{\sigma_0}\right)^n, \tag{1}$$

in which the reference strain ϵ_0 and stress σ_0 were chosen as 0.002 and 467 MPa, respectively, for both base and weld metals. Table 2 presents the estimated yield and ultimate strength for the CGHAZ, which were obtained using notched tensile specimens and corroborated with in situ tensile tests [8]; for both HIs, the strength of the weld metal was higher than that of the base metal, but the HAZs with 0.8 and 2.5 KJ/mm HIs had respectively higher and lower yield strengths than the base metal. Additionally, Fig. 1 presents a stress–strain diagram of the base metal compared to the HAZ behavior obtained from in situ tensile tests [8].

To control the microstructure sampled by the crack as it grows, the semi-K bevel geometry in Fig. 2 was selected, as recommended in the literature [9]. This bevel has been employed for evaluating HAZ toughness in multipass welds [1], and it has been standardized by BS7448 Part 2 [10]. After welding, due to the lower HI used in the root pass, the straight side of the fusion line was not perfectly perpendicular to the specimen edge, as shown in Fig. 2(right). This difficulty was overcome by removing the root pass from the specimens, as indicated in the same figure.

2.2. In situ testing

In-situ testing refers to small specimens tested inside a scanning electron microscope (“in situ”) and observed in real time. This technique has been employed in the measurement of mechanical properties of homogeneous materials and composites [11], and it demonstrated a great potential to study of inhomogeneous materials. Hence, the focus of this work was to adjust the in situ technique to HAZ specimens and compare the results with homogeneous base metal specimens.

2.2.1. Specimens

Fig. 3(left) depicts the single-edge bending specimen, SE (B), which was machined following the recommendations of BS 7448 Part 2 [10] and API RP 2Z [6], except for the minimum size requirements. The specimens were cut from welded pipes, as schematically illustrated in Fig. 3(right). To improve the dimensional accuracy of the specimen, the notch and the fatigue precrack were introduced in a larger specimen, which was later machined to dimensions indicated in 3(left). The crack front direction was radial while the crack grew in the circumferential direction (L–C direction based on BS 7448 Part 4 [10]) along the CGHAZ, as shown in Fig. 3. For comparison, specimens with homogeneous microstructures composed of only the base metal were fabricated using the same procedure.

The specimen preparation continued by polishing and etching chemically, which revealed the HAZ microstructure. In that way, the fatigue precrack and the fusion line could be identified in the optical microscope as illustrated in Fig. 4. The crack was located in the CGHAZ within a millimeter from the fusion line for both HIs. Furthermore, since the thickness of the sample was only 3 mm, the position of the crack with respect to the fusion line was not expected to vary significantly inside the specimen.

On the surface of the samples laid an 85 μm period grid obtained by evaporating lead on a mask. The purpose of the mask was to allow visualization of the deformation field. Lead provided an excellent contrast in the images, and no debonding of lead pattern was observed, even at large deformations. Similar techniques have recently been implemented [12].

2.2.2. Facilities and images

The two mobile heads of the in situ stage in Fig. 5 [13] deformed the SE (B) specimen while a load cell measured the applied load. The system worked in a vacuum at room temperature inside a Phillips 515 SEM, whose wide depth of focus and magnification range allowed observation of the general deformation of the specimen and local evolution of the CTOD in real time.

Low magnification images (11X) depict the evolution of the specimen width (W) and allow to measure the CMOD (Crack Mouth Open Displacement) and the LPD (Load Point Displacement), shown in Fig. 6(left). From higher magnification images (101X), the CTOD was directly measured as the opening between two perpendicular lines, Fig. 6 (right).

Table 2
Basic tensile properties of the HAZ calculated using notched tensile specimens [8].

HI (KJ/mm)	Yield strength (MPa)	Ultimate strength (MPa)
HAZ 0.8	514 ± 39	615 ± 36
HAZ 2.5	360 ± 28	506 ± 28

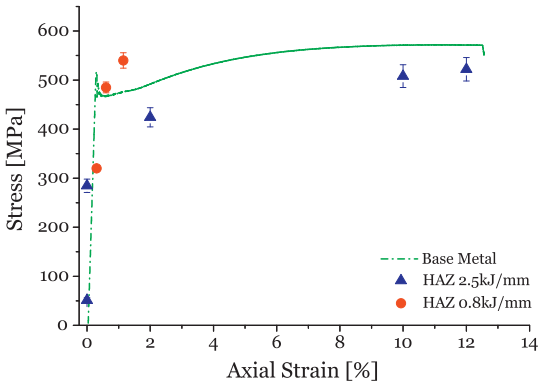

Fig. 1. Stress–Strain diagrams for the base metal and HAZ with different heat inputs [8].

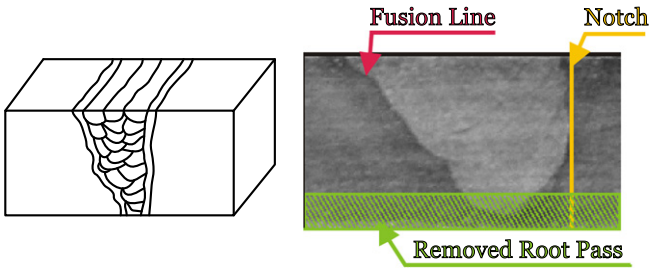

Fig. 2. Schematic semi-K bevel used for evaluating HAZ toughness (left). Micrograph of an welded bevel (right).

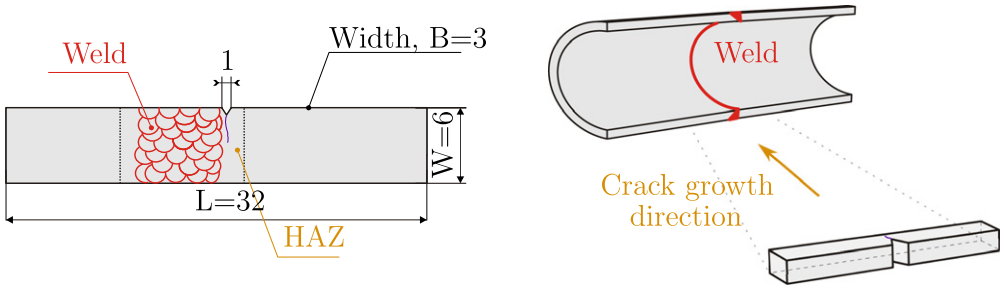

Fig. 3. (Left) Small samples used for in situ tests; dimensions are in millimeters. (Right) Specimens were obtained transversally to the weld.

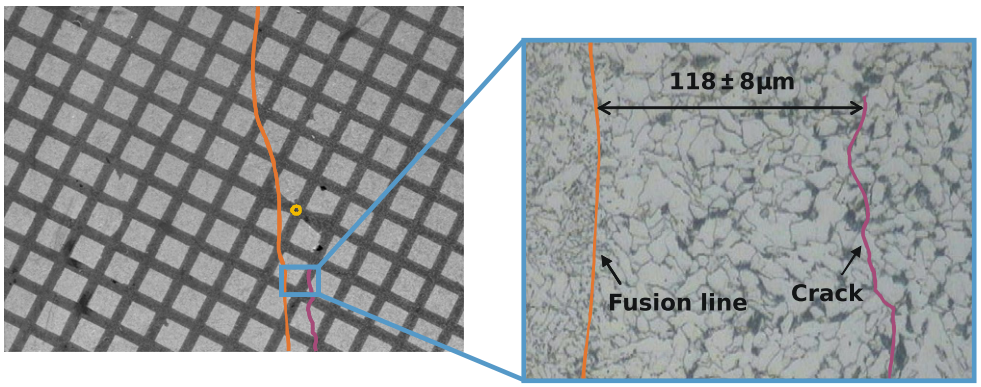

Fig. 4. Example of the location of the crack near to the fusion line for the weld with 0.8 KJ/mm. (Left) Low magnification image obtained with SEM. (Right) Optical microscope image of the CGHAZ.

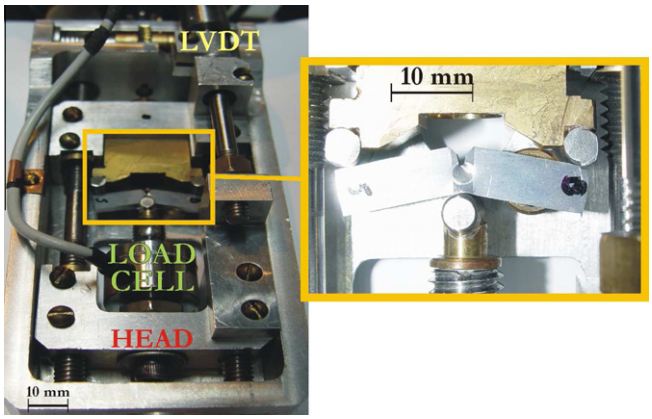

Fig. 5. Photography of the testing machine with a SE (B) specimen.

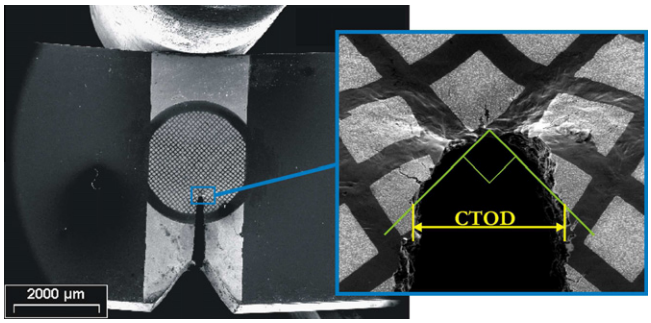

Fig. 6. Small SEN (B) specimens upon testing in the SEM. The specimen span is in the horizontal direction. (Left) SE (B) specimen at low magnification. (Right) A detail of the tip of the crack and the CTOD definition.

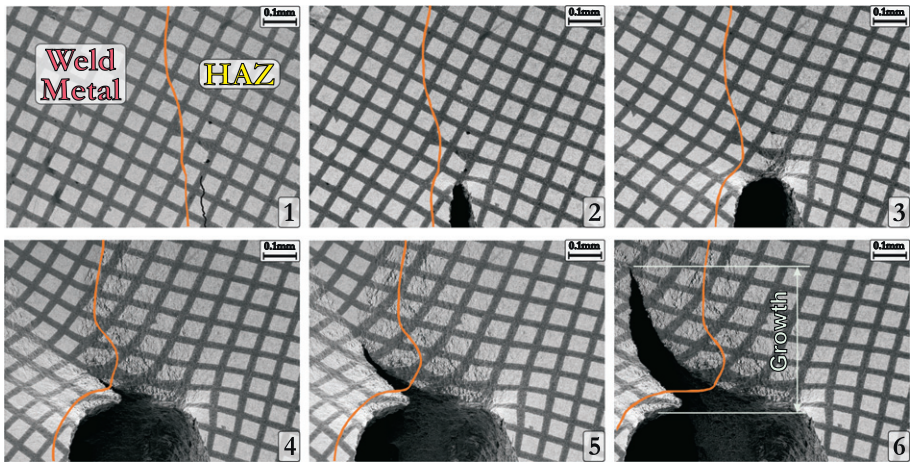

Fig. 7. Images of the crack tip from the HAZ with 0.8 KJ/mm. The CGHAZ extends approximately up to the right edge of image 1.

3. Analysis of images

Fig. 7 reproduces the sequence of the images recorded during the test of the HAZ with HI 0.8 KJ/mm. The CGHAZ lay approximately on the right edge of image 1, but rest of the HAZ extended well beyond the edge. These high magnification images (with the fusion line highlighted) show, as expected, initial crack growth due to blunting followed by tearing with a roughly constant crack tip opening angle (CTOA) between 10° and 20°. For crack growth around 0.1 mm, both mechanisms

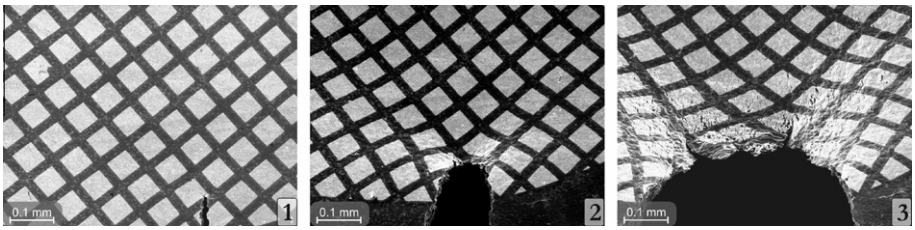

Fig. 8. Images of the crack tip from the HAZ with 2.5 KJ/mm.

were active, which indicates that before blunting was complete, the crack continued to grow because of tearing. The crack extension is considered as the projection along the initial direction of the crack (vertical direction in Fig. 7).

Fig. 8 presents a similar sequence of the images obtained during the testing of the HAZ with HI 2.5 KJ/mm, which presented more blunting at the beginning of tearing due to the lower yield strength of this HAZ [8]. For each image in the sequences, the CTOD was measured using the perpendicular-lines rule shown in Fig. 6(right). The intersection between the two lines is located at the mid-section between the surfaces of the crack and the secant to the blunt crack tip. Such a definition of the CTOD becomes less accurate with increasing crack growth, but it is an acceptable approximation for early crack growth.

Fig. 9 compares resistance curves between HAZs with various HIs until the crack tip crossed the fusion line and suggests that the HAZ with the highest HI was the toughest. For completeness, Fig. 10 compares the results from in situ tests with standardized fracture toughness tests at $-10\,^{\circ}C$ using multiple large SE (B) specimens ($12 \times 24 \times 110$ mm [7]) in which all CTOD calculations were based on BS7448 part 4. Both small and large specimens showed that the HAZ with the highest HI was the toughest, and the data seem to follow a single resistance curve for each HI.

3.1. CTOD determination

The spectrum of models that calculate the CTOD assume various underlying hypotheses (e.g., plane stress/strain, no plastic hardening, etc.), and they may not result in equivalent results. Thus, this section compares three methodologies for calculating the CTOD in Fig. 7 (0.8 KJ/mm HAZ):

- Measuring the CTOD directly from Figs. 7 and 8 using the convention proposed in Fig. 6.
- Measuring the CMOD from low magnification images and using the plastic hinge model as proposed in British Standard 7448 Part 4 [10].

$$CTOD = \left[\frac{FS}{BW^{1.5}} \cdot f\left(\frac{a_0}{W}\right)\right]^2 \cdot \frac{(1-\nu^2)}{2\sigma_0 E} + \frac{(1-r_p)\Delta a + r_p(W-a_0)}{r_p W + (1-r_p)(a_0+\Delta a)} V_P \tag{2}$$

- Obtaining the value of the J-integral using Eq. (3) taken from BS 7448 Part 4 and later calculating the CTOD using Eq. (4), which was introduced by Shih [14], who assumed that HRR fields are valid and a CTOD is defined with two perpendicular lines, as shown in Fig. 6.

$$J = \left(\left[\frac{FS}{BW^{1.5}} \cdot f\left(\frac{a_0}{W}\right)\right]^2 \cdot \frac{(1-\nu^2)}{E} + \frac{\eta_P U_P}{B \cdot (W-a_0)}\right) \cdot \left(1 - \frac{0.75\eta_P - 1}{W-a_0}\Delta a\right) \tag{3}$$

$$CTOD = d_n \cdot \frac{J}{\sigma_0} \tag{4}$$

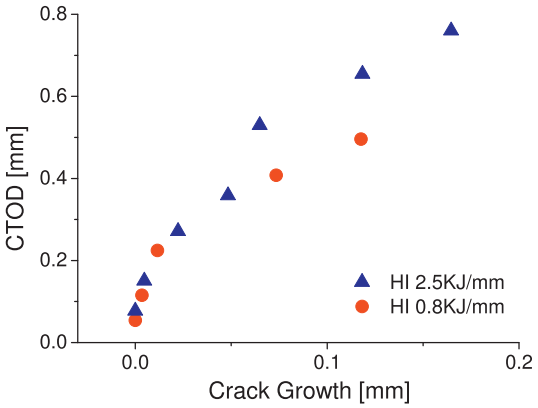

Fig. 9. Surface CTOD resistance curves measured from images for both HIs. Crack growth comprises blunting and tearing mechanisms.

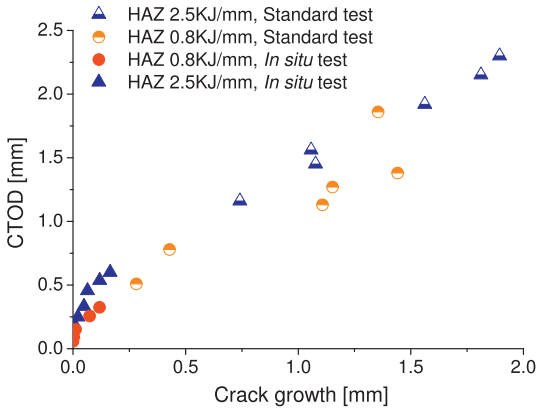

Fig. 10. Comparison between in situ and large standard fracture tests, both found using BS7448 part 4.

In these equations, F corresponds to the applied force, $\eta_P = 2$ for SE (B) specimens, the rotation factor $r_p = 0.4$, S, B, and W are specimen dimensions, a_0 and $a$are the initial and current crack lengths, respectively, E is Young's modulus, and σ_0 is the reference stress chosen as the yield strength of the base metal (467 MPa). Additionally, assuming plane stress conditions and a base metal hardening exponent of 6.8, d_n takes a value of 0.55 [14]. For comparison, a test with an homogeneous specimen (only base metal) yielded an average d_n of about 0.5, deduced from Eqs. (3) and (4) and CTOD measurements from images.

Fig. 11 presents the CTOD from the three methodologies proposed for the sequence of images in Fig. 7 (HAZ with HI 0.8 KJ/mm). The CTOD values from the images and the J-integral methodology showed good agreement in the early stages, but they disagree after crossing the fusion line; the CTOD values based on the plastic hinge were always lower than those obtained by measuring the opening directly on the images.

3.2. Strains around a crack in the HAZ

Displacement fields were computed by tabulating the location of the corners of the squares for each image, accomplished by simple inspection of the images with image editor software (a similar solution was proposed in Ref. [15]). The particle image velocimetry method employed in Ref. [8] was not satisfactory because of large deformations, rotations, and roughening of the surface. The large displacements and strains developed on the grid were described by the finite deformation formalism. Then, the deformation of each square in the deformed image was quantified by the Almansi strain tensor (E^*), which belongs to the deformed or Eulerian configuration [16].

Two coordinate systems were defined on the initial (^oz_i) and the current (z_i) configurations, and each square of the grid was parameterized using a set of convective coordinates (r, s), as presented in Fig. 12, which shows a square before and after being deformed. Traditional parametric interpolation functions provided a linear estimation of the displacements and deformations suffered by each square. This methodology assumes that the squares deform with straight sides, which is a first-order approximation that proved to be adequate in relation to the magnitude of experimental uncertainties, except perhaps for some squares next to the crack tip. See the appendix for further details about the scheme.

To assess the strain fields due to blunting, we calculated the Almansi strain tensor for each square of the grid on the images prior to tearing crack growth; this calculation was performed on images from the HAZ specimen with HI 0.8 KJ/

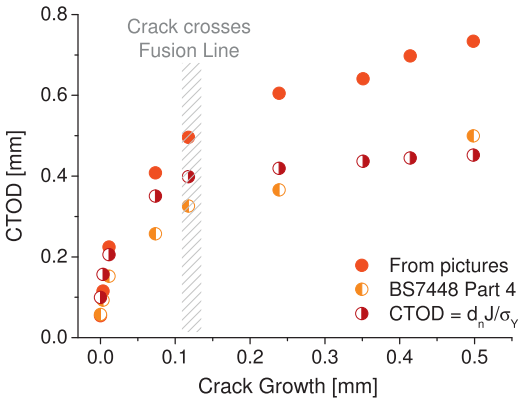

Fig. 11. CTODs obtained using three different methods for the weld with an HI of 0.8 KJ/mm. Crack growth comprises blunting and tearing mechanisms.

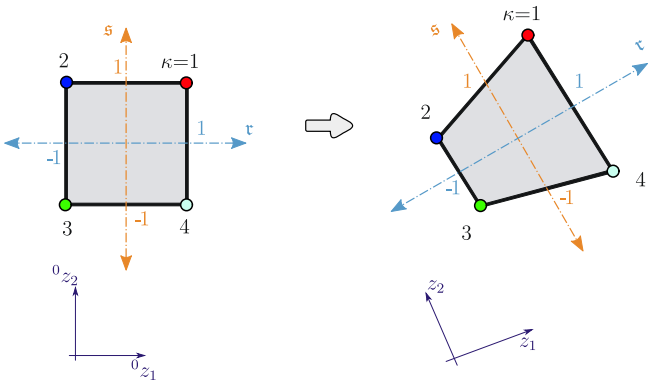

Fig. 12. Initial (Lagrangian) and current (Euclidean) coordinate systems along *i*th the parametrization of the convective coordinates.

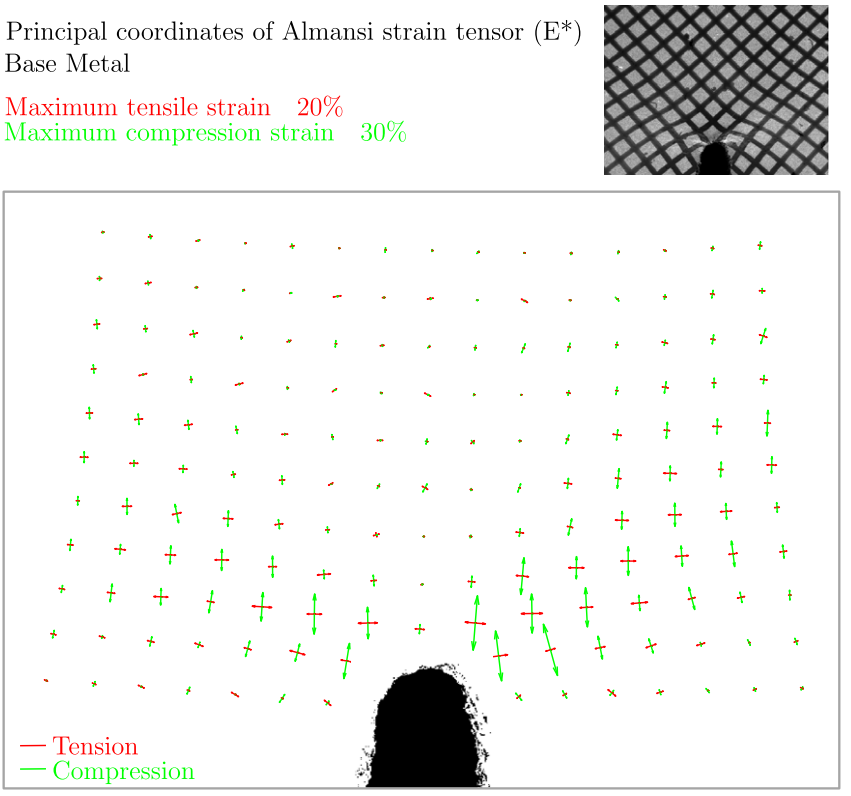

Fig. 13. Large deformation analysis of the crack tip for the base metal. Approximately symmetric strains were found in front of the crack.

mm and, for comparison, on images from homogeneous specimen composed only of base metal. Figs. 13 and 14 depict the principal values and directions of the Almansi strain tensor for the base metal and HAZ specimens, respectively.

4. Discussion

4.1. Specimen size

The application of fracture mechanics singularity models to experimental specimens is usually based on the self-similitude assumption, which requires that stress and strains fields at the crack tip are equivalent for different geometric conditions. In order to satisfy such hypothesis, standardized specimens have dimensional constraints that guarantee that the results can be transferred across multiple sizes and configurations. One of such requirements is that the specimen is big enough to reproduce the same constraint as in the application of interest. Since this requirement is sometimes not possible to be satisfied, subsize specimens have received significant attention.

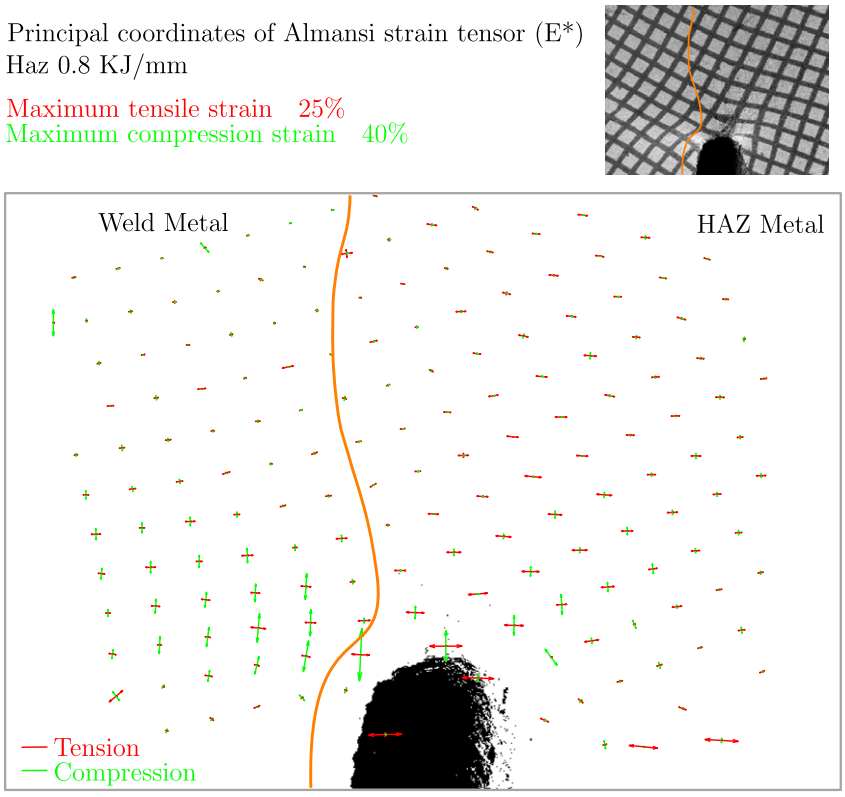

Fig. 14. Large deformation analysis of the crack tip for the weld. Note the highly asymmetric character of the strains in front of the crack.

This is an area of active research, source of multiple conferences and ASTM special technical publications (STPs) [17–19], which attempts to transfer the results from smaller fracture specimens into full size structure. Moreover, the nuclear industry has developed techniques to assess the fracture toughness of welds using subsize specimens [20]. For example, Anderson and Dodds have proposed a methodology to extrapolate the results from subsize specimens into full thickness specimens by quantifying the change in triaxiality [1]. Hence, the objective of this work is not to improve the techniques for extrapolating the fracture toughness among specimens of different size, but to assess the behavior of small specimens in comparison to traditional theoretical models.

Since fracture toughness results may depend on the dimensions of the specimen tested, the standards usually limit the maximum valid values of the CTODs as a fraction of the size of the specimen. For the dimensions of the specimens in Fig. 3, BS7448 [10] limits the maximum valid CTOD up to

$$\mathrm{CTOD}_{max} = (W - a_0)/30 = 0.1 \text{ mm}. \tag{5}$$

Such a limit is an estimation of the maximum CTOD that would uniquely characterize the material fracture toughness. Furthermore, Wallin [22] has argued there is no need for a limit in the maximum J-integral if the crack growth is limited and included in the calculation the driving force (as it is the case in Eqs. (2) and (3)). Therefore, the CTODs computed should still be valid when compared to the results of specimens with similar dimension, even more when comparing different measurements of the same specimen.

This work does not attempt to directly extrapolate the results into full-scale applications but uses small specimens to rank the initial portion of the resistance curve of different HAZs. For instance, the HAZ with an HI of 2.5 KJ/mm had a higher resistance curve than that with an HI of 0.8 KJ/mm, which is the same trend found for large specimens. Furthermore, small-scale tests provide more control in placing the crack within the HAZ and predicting the microstructure crossed by the crack with the consequent improvement in the variability of results, but without requiring as many tests as in the case of using larger specimens.

4.2. Accuracy of models

Several authors have demonstrated that fracture mechanics formulations based on homogeneous materials may not be applicable to inhomogeneous materials. For example, the J-integral may become path dependent in materials with gradients

of mechanical properties [23]. Hence, having disregarded the size of specimens as a main source of inaccuracy, this section reviews the effect of the inhomogeneous microstructure on the CTOD calculations for the three methodologies while the following section discusses the shapes of the strain fields:

Measured from images: If the faces of the crack were parallel, the CTOD could be measured at any location behind the tip, resulting in the same value. However, perpendicular lines are commonly used to measure the CTOD because the crack faces usually develop at angles. The accuracy of this correction decreases as the crack grows. However, the angle of the crack faces does not vary significantly with increasing crack growth; this minimizes the effect of the correction. Hence, the technique employed to measure the CTOD from images appears to be accurate and not influenced by the inhomogeneity. Furthermore, in situ tests can be employed for assessing the fracture toughness of materials in which indirect measurements of the CTOD may not be accurate or may be difficult to measure (e.g., graded or thin materials, respectively).

Based on the J-integral: Eqs. (3) and (4) assume that the work performed by the pins on the specimen (U_P), far from the crack, is a good measurement of the energy consumed at the crack tip. Such assumption could be violated under certain conditions (e.g., the base metal yields far from the crack tip due to a large mismatching), but that would not be the case for a weld with a moderate mismatch. Moreover, the equations have two parameters (η_P and d_n) that may be inaccurate because they are calibrated using FEM of homogeneous materials. In the literature, η_P is usually accepted as 2 for SE (B) specimens with $a/W \sim 0.5$, and although some evolution of the parameter is expected [24], the uncertainty of this value could not justify the discrepancy [25]. On the other hand, d_n, which depends on the hydrostatic condition (plane stress/strain), varies mildly with σ_0/E and strongly with the hardening coefficient n [14]. Hence, for a certain hydrostatic condition, the hardening coefficient would be the only required parameter as long as the same reference stress and Young's modulus were employed for fitting the tensile data from different materials.

The small dimensions of the specimen suggest that the plane stress condition is a good assumption, which is further supported by the average value of d_n obtained from the test of an homogeneous specimen. Moreover, the results from tensile tests indicate that the hardening coefficient of the HAZ with HI 0.8 KJ/mm is slightly higher than that of the base metal [8] while the coefficient of the weld metal is significantly higher. More hardening implies that larger values of d_n should be used in the calculation of CTOD, which yields larger values of CTOD. Hence, the local differences in hardening can justify that the J-integral method provided lower CTOD estimations than the values measured on the images. Indeed, this discrepancy increased when the crack entered the welded region (to the right of Fig. 11) because the value for d_n, assuming $n = 10$, is close to 0.7. When this value is employed to calculate the CTOD, the resulting values ar 40% larger, which agrees better with the values measured from the images.

Based on the hinge model: In this model, the rotation factor and the yield stress can be influenced by inhomogeneity, but the latter modifies only the elastic contribution that is negligible. However, the value of r_p, which is based on FEM simulations, is still a topic of discussion; even British [10] and American [26] standards use different values, 0.4 and 0.44, respectively. Moreover, a wider range of values from 0.4 to more than 0.5 have been proposed in the literature [27]. For comparison, in situ measurements with homogeneous specimens resulted in r_p values below 0.5.

If the value of the rotation center is increased up to 0.55 (i.e., moving it towards the end of the specimen), Eq. (2) yields larger values of CTOD and matches the results from the other methodologies. This shift of the rotation center may not be an actual displacement, but a phenomenon that results from using a homogeneous-based model in an inhomogeneous specimen. Furthermore, in Eq. (2), an increment of r_p has the same effect of increasing the remaining ligament, which could occur when the center of rotation is not aligned with the crack and makes the crack grow in a slanted manner, as can be seen in Fig. 7.

4.3. Strain fields

The SEM allowed the characterization of the strain fields on the surface around the crack tip. The strain field in the base metal specimen was approximately symmetric with respect to the crack plane and presented intense compression in the through thickness direction (around 30%). However, in front of the crack tip and along the direction that would follow the crack, strains are lower than 5%.

In the HAZ specimen, asymmetry developed in the strain field due to the intrinsic inhomogeneous microstructure of the region. In fact, intense compression strains developed close to the crack, especially in the weld metal region, but no significant planar deformation occurred along the path followed by the crack where strains decreased steeply and became smaller than 5% at a distance smaller than the CTOD. This plastic deformation is indeed not predicted by standard fracture theories (i.e., HRR fields), which usually result in a "kidney-shape" plastic zone. The plastically deformed region is easily observed on images 4 and 5 in Fig. 7, in which the region that deformed the most is located outside a triangular region in front of the crack tip. This deformation pattern resembles deformation bands coming out of the crack tip and turning towards the maximum shear direction.

5. Conclusions

This work presented fracture tests inside a scanning electron microscope of different HAZs from welded steel pipes. The main conclusions are summarized as follows:

- In-situ and large standardized tests seemed to follow the same resistance curve, suggesting that a single small-scale test could be employed to rank the initial portion of the resistance curves of welds.
- The main advantage of adopting in situ tests to characterize fracture toughness of welds is that the CTOD can be determined directly without using approximate models that are affected by the inhomogeneity of the HAZ. Additionally, the location of cracks can be controlled during the test as well as the type of microstructure crossed by the crack.
- The technique is also applicable to materials (e.g., graded or thin materials) in which the indirect measurements of the CTOD may not be accurate.
- The CTOD was also computed using theoretical models based on the J-integral and the plastic hinge. The results showed differences among these methods that were more pronounced after the crack crossed the fusion line, presumably because the models were devised for homogeneous materials. The J-integral appeared to be affected by local hardening at the crack tip while the plastic hinge seemed to have been affected in the location of the center of rotation.
- The deformation fields measured at the surface for base metal and HAZ specimens differed significantly, and they also differed from the field proposed by the HRR model.

Acknowledgments

The first author is grateful for the support from Comisión Nacional de Energa Atómica (CNEA), TENARIS SIDERCA and FUDETEC and the discussion and support of Richard Bravo (CINI, TENARIS) and Eduardo Dvorkin, and the technical assistance of Carlos Cotaro (CAB, CNEA).

Appendix A

A.1. Estimation of large deformations

Almansi strain tensor is defined as

$$E^*_{ij} = \frac{1}{2}\left[\frac{\delta u_i}{\delta x_j} + \frac{\delta u_j}{\delta x_i} - \frac{\delta u_k}{\delta x_i}\frac{\delta u_k}{\delta x_j}\right] \tag{A.1}$$

The small strain hypothesis neglects the non-lineal term in Eq. (A.2). The Almansi strain tensor is not just a second-order approximation but describes the problem completely. Traditional parametric interpolation functions, used to measure the strain tensor from the images, are defined as

$${}^t z_i(r,s) = h(r,s)_k\, {}^t z_i^k, \tag{A.2}$$

in which t refers to the image and k the summation of the linear interpolation functions that are defined as

$$h_1 = \frac{1}{4}(1+r)(1+s), h_2 = \frac{1}{4}(1-r)(1+s), h_3 = \frac{1}{4}(1-r)(1-s), h_4 = \frac{1}{4}(1+r)(1-s) \tag{A.3}$$

This methodology assumes that the squares deform with rigid straight sides. This is an approximation that, in general, proved to be adequate for the experimental uncertainties, except perhaps for some squares close to the crack tip.

The deformation gradient inside each square was calculated using

$${}_0{}^f X = \frac{\delta^f z_i}{\delta^f z_j} = \frac{\delta h_k}{\delta^f z_j}\, {}^f z_i^k \tag{A.4}$$

using the parametric interpolation function

$$\frac{\delta^0 z_i}{\delta r} = \frac{\delta h_k}{\delta r}\, {}^0 z_i^k \text{ and } \frac{\delta^0 z_i}{\delta s} = \frac{\delta h_k}{\delta s}\, {}^0 z_i^k \tag{A.5}$$

and defining the Jacobian matrix as:

$$[{}^0 J] = \begin{bmatrix} \frac{\delta^0 z_1}{\delta r} & \frac{\delta^0 z_2}{\delta r} \\ \frac{\delta^0 z_1}{\delta s} & \frac{\delta^0 z_2}{\delta s} \end{bmatrix}, \tag{A.6}$$

after which

$$\begin{bmatrix} \frac{\delta h_k}{\delta^0 z_1} \\ \frac{\delta h_k}{\delta^0 z_2} \end{bmatrix} = [{}^0 J]^{-1} \begin{bmatrix} \frac{\delta h_k}{\delta r} \\ \frac{\delta h_k}{\delta s} \end{bmatrix}, \tag{A.7}$$

which was combined with Eq. (A.6) to determine the deformation gradient.

References

[1] Recommended practice DNV-RP-F108. Fracture control for-pipeline installation methods-introducing cyclic plastic strain; 2006.
[2] Anderson TL. Fracture mechanics: fundamentals and applications. 3rd ed. CRC Press; 2004.
[3] Honeycombe R. Steels: microstructure and properties. 2nd ed. London;New York: Arnold Halsted Press; 1996.
[4] Kim BC, Lee S, Kim NJ, Lee DY. Microstructure and local brittle zone phenomena in high-strength low-alloy steel welds. Metall Trans A – Phys Metall Mater Sci 1991;22(1):139–49.
[5] Kim JH, Yoon EP. Notch position in the HAZ specimen of reactor pressure vessel steel. J Nucl Mater 1998;257(3):303–8.
[6] Recommended practice for preproduction qualification for steel plates for offshore structures API RP 2Z, 3rd ed., 1998.
[7] Castelluccio GM. Toughness of inhomogeneous materials: the heat affected zone in welds, masters thesis, Instituto Balseiro; 2006.
[8] Castelluccio GM, Yawny AA, Perez Ipiña JE, Ernst HA. In situ evaluation of tensile properties of Heat-Affected zones from welded steel pipes. Strain 2011;48(1):68–74.
[9] Pisarski HG. TWI research report 566/1996; 1996.
[10] BS 7448: Part 4 fracture mechanics toughness test. method for determination of fracture resistance curves and initiation values for stable crack extension in metallic materials; 1997.
[11] Perez Ipiña JE, Yawny AA. In situ observation of damage evolution and fracture toughness measurement by SEM. In: Damage prognosis. John Wiley & Sons, Ltd.; 2005. p. 61–73. http://dx.doi.org/10.1002/0470869097.ch3.
[12] Biery N, de Graef M, Pollock T. A method for measuring microstructural-scale strains using a scanning electron microscope: applications to -titanium aluminides. Metall Mater Trans A 2003;34(10):2301–13.
[13] Yawny A, Malarria J, Soukup E, Sade M. Stage for in situ mechanical loading experiments in a scanning electron microscope (Philips 515) with a small chamber. Rev Sci Instrum 1997;68(1, Part 1):150–4.
[14] Shih CF. Relationships between the J-integral and the crack opening displacement for stationary and extending cracks. J Mech Phys Solids 1981;29(4):305–26.
[15] Schroeter BM. Measurement of inhomogeneous deformation fields in polycrystalline OFHC copper, masters thesis. Atlanta, GA, USA: Georgia Institute of Technology; 2001.
[16] Malvern LE. Introduction to the mechanics of a continuous medium. Prentice Hall; 1977.
[17] Corwin W, Rosinski S, van Walle E, editors. Small specimen test techniques: third volume, STP 1329. ASTM; 1998.
[18] Sokolov M, Landes JD, editors. Small specimen test techniques: fourth volume, STP 1418. ASTM; 2002.
[19] Sokolov M, editor. Small specimen test techniques: fifth volume, STP 1502. ASTM; 2009.
[20] Corwin WR, Haggag F, Server WL, editors. Small specimen test techniques applied to nuclear reactor vessel thermal annealing and plant life extension, STP 1204. ASTM; 1994.
[1] Anderson TL, Dodds RH. Simple constraint corrections for subsize fracture toughness specimens. In: Small specimen test techniques applied to nuclear reactor vessel thermal annealing and plant life extension, STP 1204. ASTM; 1994. p. 93–105.
[22] Wallin K. Specimen size limitations in J–R curve testing–standards versus reality. In: Small specimen test techniques: fifth volume, STP 1502. ASTM; 2009. p. 1–17.
[23] Nakagaki M, Marshall CW, Brust FW. Elastic-plastic fracture mechanics evaluations of stainless steel Tungsten/Inert gas welds. In: Nonlinear fracture mechanics: volume II – elastic–plastic fracture, STP 995. ASTM; 1989. p. 214–43.
[24] Cravero S. Estimation procedure of J–R curves for SE(T) fracture specimens based upon the unloading compliance methodology, Ph.D. thesis. University of Sã o Paulo; 2007.
[25] Castelluccio GM, Cravero S, Ernst HA. Influence of weld mismatch on the structural integrity of pipes for reeling. ASME Conf Proc 2008;2008(48296):1339–46.
[26] ASTM e1820-06 standard test method for measurement of fracture toughness; 2006.
[27] Manzione PN, Perez-Ipiña JE. Plastic hinge model: a generalization to a two-dimensional situation. Fatigue Fract Engng Mater Struct 1994;17(10):1147–56.